Open-top axially swept light-sheet microscopy

BUMJU KIM,[1] MYEONGSU NA,[2] SOOHYUN PARK,[3] KITAE KIM,[2] JUNG-HOON PARK,[4] EUIHEON CHUNG,[5] SUNGHOE CHANG,[2] AND KI HEAN KIM[1,3,*]

[1] *Division of Integrative Biosciences and Biotechnology, Pohang University of Science and Technology, 77 Cheongam-ro, Nam-gu, Pohang, Gyeongbuk 37673, Republic of Korea*

[2] *Department of Physiology and Biomedical Sciences, Medical Research Center, Seoul National University College of Medicine, 103 Daehak-ro, Jongno-gu, Seoul 03080, Republic of Korea*

[3] *Department of Mechanical Engineering, Pohang University of Science and Technology, 77 Cheongam-ro, Nam-gu, Pohang, Gyeoungbuk 37673, Republic of Korea*

[4] *Department of Biomedical Engineering, Ulsan National Institute of Science and Technology (UNIST), Ulsan 44919, Republic of Korea*

[5] *Department of Biomedical Science and Engineering, Gwangju Institute of Science and Technology, Gwangju 61005, Republic of Korea*

[*]kiheankim@postech.ac.kr

Abstract: Open-top light-sheet microscopy (OT-LSM) is a specialized microscopic technique for high throughput cellular imaging of large tissue specimens including optically cleared tissues by having the entire optical setup below the sample stage. Current OT-LSM systems had relatively low axial resolutions by using weakly focused light sheets to cover the imaging field of view (FOV). In this report, open-top axially swept LSM (OTAS-LSM) was developed for high-throughput cellular imaging with improved axial resolution. OTAS-LSM swept a tightly focused excitation light sheet across the imaging FOV using an electro tunable lens (ETL) and collected emission light at the focus of the light sheet with a camera in the rolling shutter mode. OTAS-LSM was developed by using air objective lenses and a liquid prism and it had on-axis optical aberration associated with the mismatch of refractive indices between air and immersion medium. The effects of optical aberration were analyzed by both simulation and experiment, and the image resolutions were under 1.6µm in all directions. The newly developed OTAS-LSM was applied to the imaging of optically cleared mouse brain and small intestine, and it demonstrated the single-cell resolution imaging of neuronal networks. OTAS-LSM might be useful for the high-throughput cellular examination of optically cleared large tissues.

1. Introduction

High-speed optical microscopy methods, which can do the cell-level imaging of large tissue specimens, are useful for both the biological study of neuronal networks and the cellular examination of clinical tissues together with optical clearing. There are various optical microscopy techniques compatible with large tissue imaging. Light-sheet microscopy (LSM) was originally developed for the high-speed 3D imaging of tiny model organisms in developmental biology with minimal photo-damage by introducing excitation light as a sheet from the side and conducting planar imaging from the top or bottom [1–3]. LSM was later applied to the imaging of the larger samples such as optically cleared mouse brain [4]. However, LSM showed limited performance with large samples due to the degradation of image resolution with the increase of sample size. To overcome the limitation of LSM, axially swept LSM (AS-LSM) methods were developed [5–9]. AS-LSM used a tightly focused light sheet and axially swept the light sheet across the imaging FOV. Emission light generated at the focus was collected by imaging cameras in the rolling shutter mode. AS-LSM methods have been applied to the imaging of large samples such as mouse brain [7,9], bone marrow [7], spinal cord [8], and chicken embryo [9]. Another

LSM method, which shifted the light sheet axially instead of linear sweeping, was developed [10]. However, these LSM methods still had limitations on sample size due to the need for accessing the sample from multiple sides. Thus, various LSM methods were developed in different optical configurations for large sample imaging [11–13]. LS theta microscopy (LSTM) placed both the illumination and imaging arms on one side so that large samples could be placed on the other side and imaged without size limitation [11]. LSTM had the illumination arm at an oblique theta angle (less than 90°) and the imaging arm normal to the sample surface, and the light sheet scanned in the imaging plane. LSTM had relatively high image resolutions in the lateral direction and could use the full working distance of the objective lens. However, the current LSTM was in the upright configuration and had limitations in handling and imaging the samples. Unlike AS-LSM, the camera rolling shutter in LSTM was synchronized with a small portion of the scanning light sheet and the fluorescence collection was reduced. Swept confocally-aligned planar excitation (SCAPE) microscopy was another LS microscopy without sample size limitation [12,13]. SCAPE microscopy was a single objective lens system and did imaging via the oblique light sheet illumination and emission light collection along the light sheet. The tilted image plane was corrected by using an additional relay imaging arm in the matched tilted angle. Although SCAPE microscopy was simplified by using the single objective lens, the image resolution varied depending on the spatial location and it could be sensitive to optical aberrations. Various single objective lens based LSM techniques other than SCAPE microscopy have been developed [14–16]. Open-top LSM (OT-LSM) was the next LSM without sample size limitation by having separate illumination and imaging arms on one side in the inverted configuration [17–24]. The two arms were oriented at 45° with respect to the sample surface: the illumination arm at +45° and the imaging arm at -45°. OT-LSM did the planar imaging continuously with sample translation and was good for high throughput imaging. The oblique illumination and imaging with respect to the sample surface in the OT-LSM required interfacing devices such as the water prism [17,18], solid immersion lens (SIL) [19–22], and solid immersion meniscus lens (SIMlens) [23,24] for the normal incidence of illumination and emission light to the medium and the minimization of optical aberration associated with the oblique incidence of light on the interface. Standard aberration correction using the wavefront sensing and correction, and the use of an immersion objective lens without the interfacing device were implemented for high-resolution imaging [18,23]. Although the lateral resolution was improved by various methods, the axial resolution remained at approximately 4µm by using the weakly focused light sheet to cover the entire FOV in focus.

Here, we present open-top axially swept light-sheet microscopy (OTAS-LSM) for high-throughput cellular imaging of optically cleared tissues with improved axial resolution. OTAS-LSM used an electro-tunable lens (ETL) to sweep the excitation light sheet across the FOV and collected emission light from the sample by using a camera in the rolling shutter mode. The current OTAS-LSM was developed using air objective lenses in both the illumination and imaging arms and a liquid prism for the normal incidence of light onto the immersion medium and had on-axis optical aberration. The effect of aberration on image resolution was analyzed by both simulation and experiment. After the characterization of image resolution, OTAS-LSM was applied to the optically cleared mouse brain and small intestine tissues to demonstrate its high-throughput cellular imaging capability.

2. Method

2.1. System configuration of OTAS-LSM

OTAS-LSM was designed based on the configuration of water-prism OT-LSM. An ETL (EL-16-40-TC-VIS-5D-M27, Optotune) was included in the illumination arm for the axial sweeping of an excitation light sheet, and emission light from the sample was collected at an sCMOS camera

(ORCA-Flash4.0 V3 Digital CMOS camera, Hamamatsu) in the rolling shutter mode. OTAS-LSM used 10x air objective lenses (MY10X-803, NA 0.28, Mitutoyo) in both the illumination and imaging arms, which were located below the sample holder and oriented at +45° and -45° with respect to the sample surface. OTAS-LSM had the custom liquid prism filled with refractive index (RI) matching solution (C match, 1.46 RI, Crayon Technologies, Korea) for the normal light incidence onto the clearing solution.

Schematics of the OTAS-LSM system are shown in Fig. 1. A simplified optical configuration of the system, a ray tracing of the excitation light sheet in the illumination arm in two different cross-sections of x-z and y-z planes, and a detailed schematic of the liquid prism are shown. Excitation light was from either 488nm or 532nm CW lasers (Sapphire 488 LP-100, Coherent; LSR532NL-PS-II, JOLOOYO) and was delivered to the system via fiber coupling (SM1FC, Thorlabs; P1-460Y-FC-1, Thorlabs; HPUCO-23-532-sm-4.5as, Oz Optics). Excitation light from the fiber was collimated by a lens (L1, AC254-040-A, Thorlabs). The collimated excitation beam was converted to a sheet beam by a cylindrical lens (LJ1695RM-A, Thorlabs). The sheet beam was relayed to the sample by using two lens pairs of L2 (AC254-100-A, Thorlabs) and L3 (AC254-200-A, Thorlabs), and L4 (AC254-150-A, Thorlabs) and the objective lens. The ETL was placed between the first lens pair (L2 and L3) to control the collimation of sheet beam in the Fourier plane and to change the axial position of the sheet beam in the sample. The width of excitation sheet beam before the objective lens was approximately the same size as the back aperture of the objective lens to generate the light sheet beam with the full numerical aperture (NA) of the objective lens (0.28NA). The light sheet after the objective lens was designed to be approximately 2.1mm wide and 0.8μm thick at the beam waist in full width at half maximum (FWHM), and the focus of light sheet was 25μm long. Excitation light from the air objective lens entered the sample through the liquid prism. The liquid prism formed the interface of RI matching solution for the normal incidence of excitation light.

Excitation light passed through the RI matching solution in the liquid prism, a quartz coverslip (Round quartz coverslip, Ted Pella) at the bottom of the sample holder, and then got focused in the sample immersed in the RI matching solution. The quartz coverslip was used owing to its matched RI (1.46) with the RI matching solution. Emission light generated in the sample by the excitation light sheet was collected at the imaging arm, oriented orthogonally with respect to the illumination arm. Emission light in the sample passed through the sample holder and the liquid prism and was collected by the other air objective lens. After the objective lens, emission light passed through an emission filter (ET525LP and ET542LP, Chroma) and a camera lens (A17 AF 70-300mm F4-5.6 Di LD MACRO 1:2, Tamron) and then was collected at the sCMOS camera. The camera lens worked as a variable tube lens with adjustable focal length from 180mm to 300mm. The sCMOS camera collected emission light in the rolling shutter mode. The speed of the rolling shutter and the exposure time of the camera were adjusted to be matched with the sweeping speed of excitation light sheet in the sample for confocal gating. The collected image data was transferred to a data acquisition computer via a frame grabber (Firebird camera link frame grabber, Active silicon). A motorized sample stage (MS-2000 FLAT-TOP XY automated stage, ASI) was used to translate the specimen between each frame. The planar imaging of the specimen at the oblique angle with respect to the sample surface was conducted synchronously with the stepwise sample translation.

The custom liquid prism was used in the OTAS-LSM. The liquid prism was in the shape of a right-angled prism made of aluminum, and regular coverslips were glued onto the right-angled sides as windows. Its size was 8.5mm long on the right-angled side. The liquid prism held the RI matching solution. The imaging FOV was approximately 1mm × 1mm with 2048 × 2048 pixels, and the lateral resolution was approximately 0.8μm without aberration. Since the illumination light sheet was oriented at 45° to the sample surface, the 1mm × 1mm FOV corresponded to 0.67mm × 1mm in the depth and width axes. For the axial scanning of light sheets, various
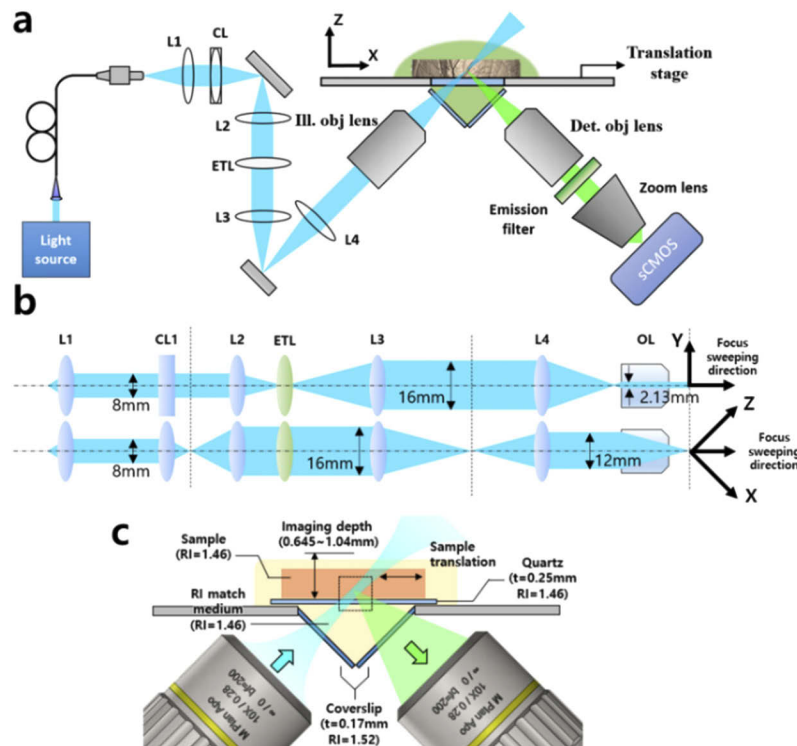
Fig. 1. Schematics of OTAS-LSM. (a) An overall schematic of OTAS-LSM, (b) A detail optical configuration of the illumination arm, (c) A detail schematic of the sample interface.

actuation methods have been implemented [7]. The ETL was used in the current system for the simple optical configuration and a high imaging speed up to 30 fps. The ETL is known to induce optical aberration at some level due to the geometric constraint of the lens surface. However, the aberration effect might be negligible in the current system because the target resolution was not high. A custom LabView program was developed to control the imaging process. The program generated an analog voltage output signal to control the ETL driver, and a digital trigger output signal to initiate the rolling shutter of the sCMOS camera, and a digital output signal to move the microscope stage. The analog voltage signal for the ETL was in a Sawtooth waveform consisting of a linear ramp section (25ms) and a return and rest section (8ms). The return and rest section was to stabilize the ETL before the next scan. The Sawtooth waveform was 33ms in total and repeated during the imaging.

2.2. System characterization by aberration simulation and measurement

The current OTAS-LSM design had on-axis optical aberration by using the air objective lenses and the liquid prism. The refractive index mismatch of the air and the RI matching solution in the light path caused the aberration. The aberration was analyzed by both simulation and experiment. All the analysis and processing were performed using MATLAB (Mathworks Inc, Natick, Massachusetts). A custom MATLAB code was developed for the simulation and a simple ray tracing method was used in the analysis. Light rays, which launched in parallel to the optical axis before the back aperture of the objective lens, experienced multiple refractions by passing through the layers of different RIs including the air, coverslip, RI matching solution until arriving at a point (z) in the optical axis. Path length of the ray to the point in the optical axis was calculated by adding individual path length segments multiplied with the corresponding

RIs. Path length differences (PLDs) among the rays at different radial positions in the plane of objective back aperture (r_{ap}) were obtained. Light intensity at the point in the optical axis was calculated by combining the rays. The geometrical coordinate (z=0) was set at the focus of the light rays in the aberration-free condition. The axial location of the maximum intensity was found, and it was set to be the focus in the aberration condition. The PLDs among the rays to the focus were analyzed by using Zernike polynomials. Dominant Zernike coefficients in the current system were ones of defocus and spherical aberration. The obtained spherical aberration coefficient was used to construct the point spread function (PSF) in the aberration condition.
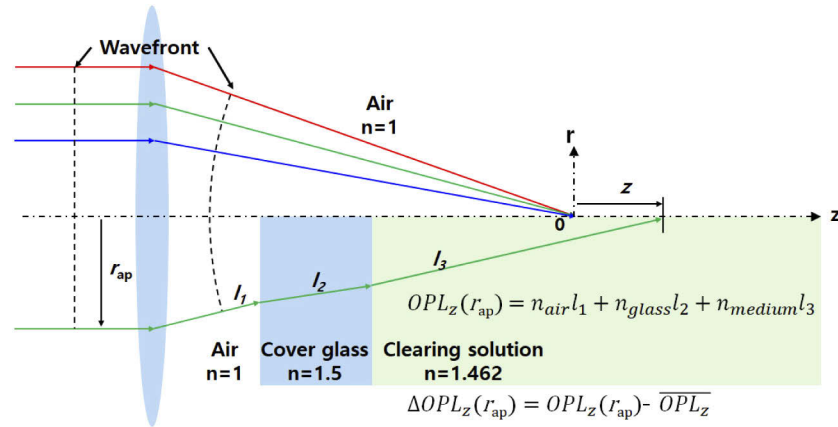

Fig. 2. A ray diagram for the aberration analysis of OTAS-LSM. The upper half is the ideal case without RI mismatch, and the lower half is the actual case where light rays travel through the layers of different RIs. A ray launched parallel to the optical axis experienced multiple refractions by going through the layers of different RIs. Path length of the ray was calculated by adding up the individual length segments multiplied with the corresponding RIs.

The imaging resolution was experimentally measured by imaging fluorescent microspheres (0.5 µm in diameter) embedded in the agarose and RI matching solution mixture. The intensity profiles of the microsphere images were obtained and fitted to the Gaussian function to analyze full width at half maximum intensity (FWHM). More than 10 microsphere images were analyzed, and the average FWHM values were obtained.

2.3. Sample preparation of optically cleared tissues and OTAS-LSM imaging

After the characterization, OTAS-LSM was applied to the imaging of optically cleared tissues including the brain slices of Thy1-eYFP mice and the small intestines of ChAT-Cre Tomato knock-in mice, *ex vivo*. All animal procedures in this study were approved by the Institutional Animal Care and Use Committee (POSTECH-2019-0061). In the mouse brain sample preparation, mice were euthanized by injection with a zoletil and rompun mixture before intracardiac perfusion and then perfused with 20ml of PBS and 20ml 4% paraformaldehyde (PFA) using a peristaltic pump. The fixed mouse brain was sliced coronally in 1 mm thickness. The brain slices were incubated in the RI matching solution at 36°C for 2 hours for the optical clearing. The RI matching solution increased tissue transparency by matching the RI of the fixed brain tissue. In the small intestine case, mice were euthanized by the same method above and the small intestine tissues were extracted and excised. The extracted tissues were incubated in PFA solution for 24 hours and then in the RI matching solution at 36 °C for 6 hours.

The optically cleared tissue specimens were mounted in the sample holder of OTAS-LSM and imaged in 3D with the sample translation in both the x and y directions. The tissue specimens

were imaged in the unit of long image strips which were generated with the translation in the x direction in the step size of 1µm. In the case of mouse brain slice, 12 image strips in total were acquired to cover the entire area. Total imaging time was approximately 1 hour (67 minutes). The acquired image data was processed for 3D reconstruction. The raw image data was sheared at 45° to the sample surface, and an image processing algorithm was developed to transform the image data in the xyz coordinate. Before the transformation, the raw images were enhanced by using Richardson–Lucy deconvolution method. An aberrated system PSF, which was generated computationally from the aberration simulation, was used as an input in the deconvolution. The deconvolution was iterated for 10 times. The enhanced image data was used in the transformation. A 3D matrix with a fine pixel spacing, which was compatible with the spacing in the sheared image, was created and filled with the image data in the correct coordinate. The matrix still had empty pixels owing to the fine spacing and the empty pixels were filled by interpolating the intensities of neighboring pixels with the consideration of image PSF shape. After all the pixels were filled, the matrix was resized with the proper shrinkage and aspect ratios. Planar images in the en-face (xy) and cross-sectional (xz) planes could be accessed. Each image strip became 1mm × 0.67mm in the cross-section (width × height) after the transformation. The image strips were joined manually by estimating the overlap and relative coordinates in a 3D rendering software. The final reconstructed volumetric image was 11.4mm × 8.1mm × 0.67mm in width × height × thickness. In the case of mouse small intestine specimens, 8 image strips were acquired in total. The imaging time was approximately 30 minutes. The acquired image data was processed in the same ways described above. The reconstructed volumetric image was approximately 8mm × 4mm × 0.67mm in width × height × thickness.

2.4.   Confocal microscopy imaging for comparison with OTAS-LSM

OTAS-LSM was compared with confocal microscopy in the mouse brain. Confocal imaging was conducted by using a commercial system (SP-5, Leica). A multi-immersion 20x objective lens (HC PL Apo 20x/0.7 Imm, Leica) was used for the imaging in the RI matching solution. The theoretical image resolution was 0.27µm and 1.83µm in the transverse and axial directions, respectively. The imaging field of view (FOV) was 258µm × 258µm consisting of 1024 × 1024 pixels. Volumetric images were acquired with the axial step size of 1µm and the imaging speed of 2 frames/s. The imaging time for 1mm^3 volume was approximately 1 hr.

3.   Results

3.1.   Aberration analysis of OTAS-LSM

The results of image resolution analysis in OTAS-LSM are shown in Fig. 2. A schematic showing the illumination and imaging light paths and the geometrical coordinates are shown in Fig. 3(a). The simulation and experiment results are shown in Fig. 3(b) and 3(c), respectively. In the simulation, the changes of excitation light sheet, imaging PSF, and system PSF by the aberration were analyzed. The excitation light sheet, which was 0.73 µm thick in FWHM in the aberration-free condition, was degraded to 1.00 µm with the aberration. The imaging PSF, which was 0.79 µm in FWHM in the aberration-free condition, was degraded to 1.06 µm with the aberration. The system PSF could be obtained by multiplying the axially swept illumination light sheet and the imaging PSF that crossed each other just like those in the schematic. The results in both the aberration-free and aberration conditions are shown in Fig. 3(b). The system resolutions, which were 1.14 µm in the x-z plane and 0.79 µm in the y axis in the aberration-free condition, were degraded to 1.50 µm, 1.06 µm with the aberration, respectively. The image resolution of the OTAS-LSM was degraded to approximately 131% of the theoretical values.

In the experiment, the PSF of microspheres was measured to be 1.60 ± 0.17 µm and 1.58 ± 0.15 µm in FWHM in the x-z plane and 1.49 ± 0.04 µm in the y axis, respectively.
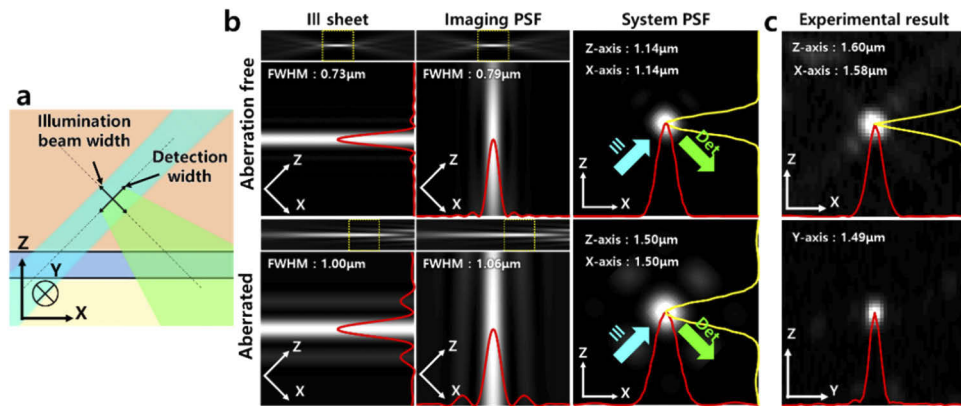
Fig. 3. Resolution analysis in both simulation and experiment. (a) A schematic showing the excitation light sheet, emission light path, and the geometrical coordinates (b) Simulation results of excitation light sheet, detection point spread function (PSF), and system PSF in both the aberration-free and aberration conditions. (c) Experimental results showing representative images of a 0.5 µm fluorescent microsphere and intensity profiles.

The measured image resolutions were 106.6% (x), 105.3% (z), and 140.5% (y) of the simulation results with the aberration, and approximately 140% (x, z) and 188.6% (y) of the aberration-free theoretical results. The actual resolutions were expected to be smaller than the measurement results, which had additional pixelation errors of the camera whose pixel spacing was 0.46 µm. The analysis concluded that the image resolutions of the OTAS-LSM system were 1 to 2 µm in both the simulation and experiments and applicable for single-cell resolution imaging.

3.2. *OTAS-LMS imaging of optically cleared mouse brain and mouse small intestine*

After the system characterization, OTAS-LSM was applied to optically cleared tissues including the mouse brain and small intestine for the cell-level visualization of neuronal networks. Thy1-eYFP mice expressing eYFP in motor and sensory neurons were used for the imaging of neural networks in the brain. ChAT-Cre-tdTomato knock-in mice expressing tdTomato fluorescent protein in the cholinergic innervation and nonneuronal acetylcholine-synthesizing cells in the periphery were used for the imaging of enteric nervous system in the small intestine [25]. OTAS-LSM images of the mouse brain slice are shown in Fig. 4. An image of the entire brain slice and magnified images in the several regions of interest (ROIs) are shown. These images were volumetric images with depth color coding. The gross image in Fig. 4(a) was color coded in the depth range from 0µm to 200µm deep from the surface, and the magnified images in Fig. 4(b-d) were coded in the range from 0µm to 100µm deep from the surface. The image of entire mouse brain slice showed a gross neural network in the mouse brain: sparse network in the cerebral cortex and dense network in the hippocampus. The magnified images in 3 different mouse brain ROIs showed complex neural networks at the single-cell level. The magnified image in the cerebral cortex in Fig. 4(b) showed pyramidal cells with apical dendrites extending upward towards the cortical surface. The apical dendrites branched out several times in the extension. The image in the CA1 region of the hippocampus in Fig. 4(c) showed pyramidal cells with apical dendrites arising from the soma in the stratum pyramidale and extending down to stratum radiatum and lacunosum-moleculare. The magnified image in the thalamus in Fig. 4(d) showed nerve fibers projecting out to the cerebral cortex. Individual nerve fibers were resolved. OTAS-LSM visualized the neural network of the mouse brain at the resolution of individual neurons.
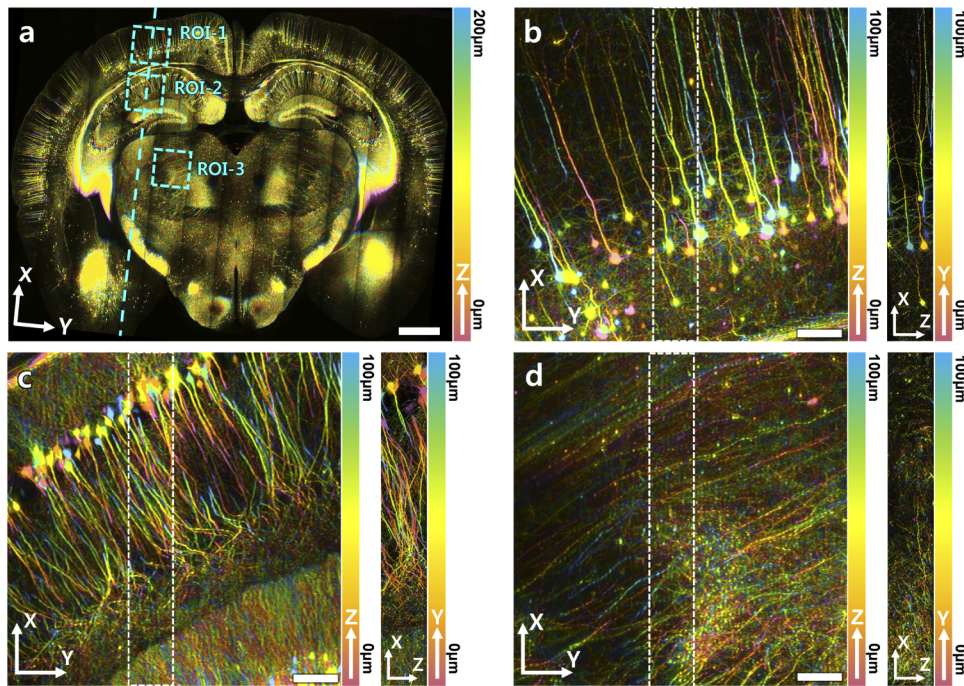
Fig. 4. OTAS-LSM images of an optically cleared Thy1-eYFP mouse brain. (a) A large sectional image of the brain slice with depth color coding from 0 to 200μm. (b-d) Magnified images of the cerebral cortex, hippocampus, and thalamus with depth color coding from 0 to 100μm, respectively. Scale bars: 1mm in (a), 100μm in (b-d).

OTAS-LSM images of the enteric nervous system (ENS) in the mouse small intestine are shown in Fig. 5. A 3D image in the large FOV and three magnified images in the respective ROIs are shown in Fig. 5(a) and 5(b-c), respectively. The large FOV image was presented in depth color coding, and the magnified images were presented as the maximum intensity projection (MIP) of the 3D image in specific depth ranges. The large FOV image showed the gross structure of ENS. Neuronal networks in different morphologies or structures appeared at different depth ranges. The magnified images showed the myenteric plexus (0 – 20μm), deep muscular plexus. (20 – 30μm), and submucosal plexus (30 – 40μm).

3.3. Comparison of OTAS-LSM with confocal microscopy in the mouse brain

OTAS-LSM was compared with confocal microscopy (CM) in the imaging of mouse brain, and the results are in Fig. 6. Both the OTAS-LSM and CM images in two different regions of the mouse brain, the cerebral cortex (Fig. 6(a) and (b)) and hippocampus (Fig. 6(c) and (d)), are shown. Both OTAS-LSM and CM images were in the same FOV of 260μm × 260μm. CM visualized fine cellular structures down to thin dendrites (Fig. 6(b) and (d)) with the higher image resolution compared to those of OTAS-LSM. However, OTAS-LSM could resolve individual neurons at the modest image resolution of 1-2μm (Fig. 6(a) and (c)). In terms of imaging throughput, OTAS-LSM could image faster than CM proportionally to the image resolution. CM needed extra time for switching the imaging sections for large sectional imaging: approximately 1s per switching. On the other hand, OTAS-LSM could do the 3D imaging continuously without the need of extra time for the switching. OTAS-LSM had an advantage for the high throughput visualization of gross cellular structure of the optically cleared tissues.
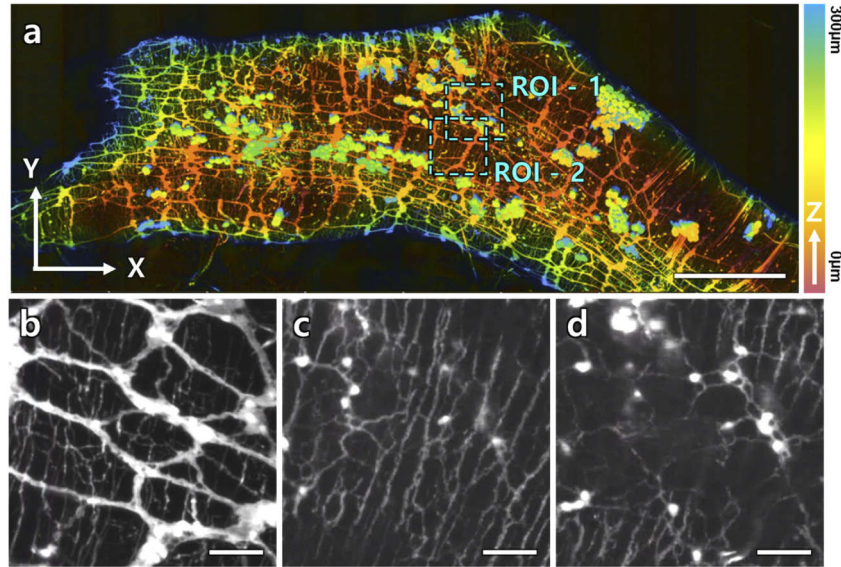
Fig. 5. OTAS-LSM images of an optical cleared small intestine of the ChAT-Cre-tdTomato knock-in mouse. (a) A large sectional image with depth color coding from 0 to 300μm. (b-d) Magnified images of the region of interests (ROIs) marked in the large sectional image and processed as maximum intensity projection (MIP). (b) An MIP image of ROI-1 showing the myenteric plexus from 0 to 20μm from the surface. (c) and (d) are MIP images of the deep muscular plexus from 20 to 30μm in depth and submucosal plexus from 30 to 40μm in depth. Scale bars are 1mm in (a) and 100μm in (b-d).
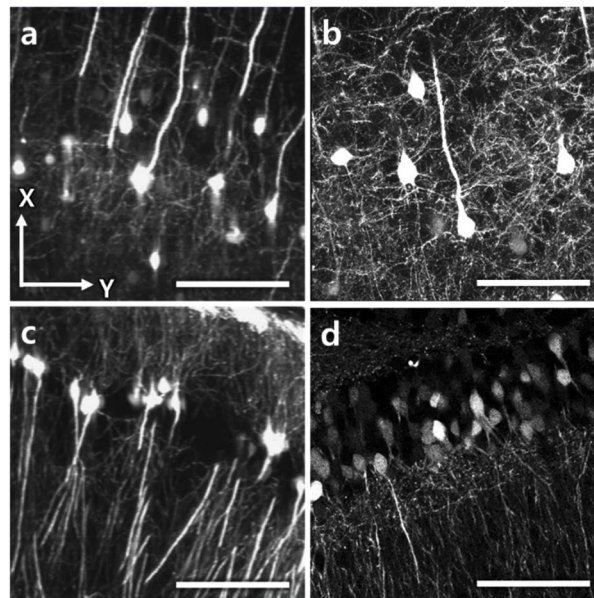

Fig. 6. Comparison between OTAS-LSM and confocal microscopy (CM) in the visualization of neuronal network in the brain. (a, b) MIP OTAS-LSM and CM images of the cerebral cortex, respectively. (c, d) MIP OTAS-LSM and CM images of the hippocampus. Scale bars: 100μm.

4. Discussion

OTAS-LSM was developed for the high throughput imaging of optically cleared tissues with improved axial resolution. The current OTAS-LSM was based on the water-prism OT-LSM design. OTAS-LSM implemented the axial sweeping of the excitation light sheet by using the ETL. The emission light generated at the focus of light sheet was collected confocally by synchronizing the rolling shutter in the imaging camera with the excitation light sheet. The imaging FOV was approximately 1mm × 1mm in the oblique imaging plane, and the imaging speed was 30 frames/s. Although the current OTAS-LSM had the inherent on-axis optical aberration by using the air objective lenses and the liquid prism, the image resolution was 1-2μm in both the axial and transverse directions. In the imaging of optically cleared mouse brain and small intestine tissues, OTAS-LSM demonstrated its ability of visualizing the neural network in the mouse brain and the ENS in the small intestine in the single-cell level.

The current OTAS-LSM had several limitations including the imaging depth range, the image resolution, and the imaging speed. The current system could image the sample down to less than 1 mm deep from the surface, because the sample holder could not change the axial position of the sample with respect to the illumination and imaging paths. A new sample holder, which could axially translate the sample, would increase the imaging depth range [23]. The new sample holder together and a new immersion chamber are currently under development. The current system had the on-axis optical aberration, and the aberration would be worsened with the imaging depth. The resolution could be improved by adapting aberration correction methods. Wavefront correction devices such as a deformable mirror (DM) or a spatial light modulator (SLM) could be incorporated [18,26,27]. The current imaging speed was up to 30 frames/s, limited by the ETL. Other devices such as deformable mirrors, which have the faster response, could be used both to axially sweep the light sheet and to correct aberration. The current OTAS-LSM was configured with single excitation lasers at a time. Multi-color imaging would be implemented in the future by using multiple excitation lasers. Light sheets of different wavelengths might get focused at different axial locations due to chromatic aberration from the ETL and the liquid prism in the illumination path. The focal position of different wavelength light sheets would need to be measured to adjust the ETL waveform amplitude. The current OTAS-LSM might not be sensitive to the focus mismatch of different wavelength light sheets, because the excitation focus was approximately 25 μm long.

5. Conclusion

OTAS-LSM was developed for the high-throughput cellular imaging of optically cleared large tissues at the improved axial resolution. OTAS-LSM was implemented by using an ETL for the axial sweeping, and air objective lenses and the liquid prism for illumination and imaging. The image resolution of OTAS-LSM was 1 to 2 μm with some degradation associated with the on-axis optical aberration. The performance of OTAS-LSM was verified in the imaging of the optically cleared mouse brain and small intestine and it could visualize neuronal network at the cellular level. OTAS-LSM might be useful for the cellular examination of optically cleared tissues by providing cellular information at high throughputs.

Disclosures. The authors declare no conflicts of interest.

References

1. J. Huisken, J. Swoger, F. Del Bene, J. Wittbrodt, and E. H. K. Stelzer, "Optical sectioning deep inside live embryos by selective plane illumination microscopy," Science **305**(5686), 1007–1009 (2004).
2. P. J. Keller, A. D. Schmidt, J. Wittbrodt, and E. H. Stelzer, "Reconstruction of zebrafish early embryonic development by scanned light sheet microscopy," Science **322**(5904), 1065–1069 (2008).

3. M. B. Ahrens, M. B. Orger, D. N. Robson, J. M. Li, and P. J. Keller, "Whole-brain functional imaging at cellular resolution using light-sheet microscopy," Nat. Methods **10**(5), 413–420 (2013).

4. H. U. Dodt, U. Leischner, A. Schierloh, N. Jahrling, C. P. Mauch, K. Deininger, J. M. Deussing, M. Eder, W. Zieglgansberger, and K. Becker, "Ultramicroscopy: three-dimensional visualization of neuronal networks in the whole mouse brain," Nat. Methods **4**(4), 331–336 (2007).

5. K. M. Dean, P. Roudot, E. S. Welf, G. Danuser, and R. Fiolka, "Deconvolution-free Subcellular Imaging with Axially Swept Light Sheet Microscopy," Biophys. J. **108**(12), 2807–2815 (2015).

6. P. N. Hedde and E. Gratton, "Selective plane illumination microscopy with a light sheet of uniform thickness formed by an electrically tunable lens," Microsc. Res. Tech. **81**(9), 924–928 (2018).

7. T. Chakraborty, M. K. Driscoll, E. Jeffery, M. M. Murphy, P. Roudot, B. J. Chang, S. Vora, W. M. Wong, C. D. Nielson, H. Zhang, V. Zhemkov, C. Hiremath, E. D. De La Cruz, Y. Yi, I. Bezprozvanny, H. Zhao, R. Tomer, R. Heintzmann, J. P. Meeks, D. K. Marciano, S. J. Morrison, G. Danuser, K. M. Dean, and R. Fiolka, "Light-sheet microscopy of cleared tissues with isotropic, subcellular resolution," Nat. Methods **16**(11), 1109–1113 (2019).

8. J. Ping, F. Zhao, J. Nie, T. Yu, D. Zhu, M. Liu, and P. Fei, "Propagating-path uniformly scanned light sheet excitation microscopy for isotropic volumetric imaging of large specimens," J. Biomed. Opt. **24**(08), 1–5 (2019).

9. F. F. Voigt, D. Kirschenbaum, E. Platonova, S. Pages, R. A. A. Campbell, R. Kastli, M. Schaettin, L. Egolf, A. van der Bourg, P. Bethge, K. Haenraets, N. Frezel, T. Topilko, P. Perin, D. Hillier, S. Hildebrand, A. Schueth, A. Roebroeck, B. Roska, E. T. Stoeckli, R. Pizzala, N. Renier, H. U. Zeilhofer, T. Karayannis, U. Ziegler, L. Batti, A. Holtmaat, C. Luscher, A. Aguzzi, and F. Helmchen, "The mesoSPIM initiative: open-source light-sheet microscopes for imaging cleared tissue," Nat. Methods **16**(11), 1105–1108 (2019).

10. L. Gao, "Extend the field of view of selective plan illumination microscopy by tiling the excitation light sheet," Opt. Express **23**(5), 6102–6111 (2015).

11. B. Migliori, M. S. Datta, C. Dupre, M. C. Apak, S. Asano, R. Gao, E. S. Boyden, O. Hermanson, R. Yuste, and R. Tomer, "Light sheet theta microscopy for rapid high-resolution imaging of large biological samples," BMC Biol. **16**(1), 57 (2018).

12. V. Voleti, K. B. Patel, W. Li, C. Perez Campos, S. Bharadwaj, H. Yu, C. Ford, M. J. Casper, R. W. Yan, W. Liang, C. Wen, K. D. Kimura, K. L. Targoff, and E. M. C. Hillman, "Real-time volumetric microscopy of in vivo dynamics and large-scale samples with SCAPE 2.0," Nat. Methods **16**(10), 1054–1062 (2019).

13. M. B. Bouchard, V. Voleti, C. S. Mendes, C. Lacefield, W. B. Grueber, R. S. Mann, R. M. Bruno, and E. M. Hillman, "Swept confocally-aligned planar excitation (SCAPE) microscopy for high speed volumetric imaging of behaving organisms," Nat. Photonics **9**(2), 113–119 (2015).

14. C. Dunsby, "Optically sectioned imaging by oblique plane microscopy," Opt. Express **16**(25), 20306–20316 (2008).

15. M. Kumar and Y. Kozorovitskiy, "Tilt-invariant scanned oblique plane illumination microscopy for large-scale volumetric imaging," Opt. Lett. **44**(7), 1706–1709 (2019).

16. E. Sapoznik, B. J. Chang, J. Huh, R. J. Ju, E. V. Azarova, T. Pohlkamp, E. S. Welf, D. Broadbent, A. F. Carisey, S. J. Stehbens, K. M. Lee, A. Marin, A. B. Hanker, J. C. Schmidt, C. L. Arteaga, B. Yang, Y. Kobayashi, P. R. Tata, R. Kruithoff, K. Doubrovinski, D. P. Shepherd, A. Millett-Sikking, A. G. York, K. M. Dean, and R. P. Fiolka, "A versatile oblique plane microscope for large-scale and high-resolution imaging of subcellular dynamics," Elife **9**, e57681 (2020).

17. R. McGorty, H. Liu, D. Kamiyama, Z. Dong, S. Guo, and B. Huang, "Open-top selective plane illumination microscope for conventionally mounted specimens," Opt. Express **23**(12), 16142–16153 (2015).

18. R. McGorty, D. Xie, and B. Huang, "High-NA open-top selective-plane illumination microscopy for biological imaging," Opt. Express **25**(15), 17798–17810 (2017).

19. A. K. Glaser, N. P. Reder, Y. Chen, E. F. McCarty, C. Yin, L. Wei, Y. Wang, L. D. True, and J. T. C. Liu, "Light-sheet microscopy for slide-free non-destructive pathology of large clinical specimens," Nat. Biomed. Eng. **1**(7), 0084 (2017).

20. Y. Chen, W. Xie, A. K. Glaser, N. P. Reder, C. Mao, S. M. Dintzis, J. C. Vaughan, and J. T. C. Liu, "Rapid pathology of lumpectomy margins with open-top light-sheet (OTLS) microscopy," Biomed. Opt. Express **10**(3), 1257–1272 (2019).

21. L. A. Barner, A. K. Glaser, L. D. True, N. P. Reder, and J. T. C. Liu, "Solid immersion meniscus lens (SIMlens) for open-top light-sheet microscopy," Opt. Lett. **44**(18), 4451–4454 (2019).

22. L. A. Barner, A. K. Glaser, H. Huang, L. D. True, and J. T. C. Liu, "Multi-resolution open-top light-sheet microscopy to enable efficient 3D pathology workflows," Biomed. Opt. Express **11**(11), 6605–6619 (2020).

23. A. K. Glaser, N. P. Reder, Y. Chen, C. Yin, L. Wei, S. Kang, L. A. Barner, W. Xie, E. F. McCarty, C. Mao, A. R. Halpern, C. R. Stoltzfus, J. S. Daniels, M. Y. Gerner, P. R. Nicovich, J. C. Vaughan, L. D. True, and J. T. C. Liu, "Multi-immersion open-top light-sheet microscope for high-throughput imaging of cleared tissues," Nat. Commun. **10**(1), 2781 (2019).

24. A. K. Glaser, K. W. Bishop, L. A. Barner, R. B. Serafin, and J. T. C. Liu, "A hybrid open-top light-sheet microscope for multi-scale imaging of cleared tissues," BioRxiv (2020).

25. L. Gautron, J. M. Rutkowski, M. D. Burton, W. Wei, Y. Wan, and J. K. Elmquist, "Neuronal and nonneuronal cholinergic structures in the mouse gastrointestinal tract and spleen," J. Comp. Neurol. **521**(16), 3741–3767 (2013).

26. C. Bourgenot, C. D. Saunter, J. M. Taylor, J. M. Girkin, and G. D. Love, "3D adaptive optics in a light sheet microscope," Opt. Express **20**(12), 13252–13261 (2012).

27. D. Wilding, P. Pozzi, O. Soloviev, G. Vdovin, and M. Verhaegen, "Adaptive illumination based on direct wavefront sensing in a light-sheet fluorescence microscope," Opt. Express **24**(22), 24896–24906 (2016).